

# Lawrence Berkeley National Laboratory

## LBL Publications

### Title

Understanding slow-moving landslide triggering processes using low-cost passive seismic and inclinometer monitoring

### Permalink

<https://escholarship.org/uc/item/30622458>

### Authors

Fiolleau, Sylvain

Uhlemann, Sebastian

Wielandt, Stijn

et al.

### Publication Date

2023-08-01

### DOI

10.1016/j.jappgeo.2023.105090

### Copyright Information

This work is made available under the terms of a Creative Commons Attribution License, available at <https://creativecommons.org/licenses/by/4.0/>

Peer reviewed



# Understanding slow-moving landslide triggering processes using low-cost passive seismic and inclinometer monitoring

Sylvain Fiolleau<sup>\*</sup>, Sebastian Uhlemann, Stijn Wielandt, Baptiste Dafflon

Lawrence Berkeley National Laboratory, Earth and Environmental Sciences Area, Berkeley, CA, USA

## ARTICLE INFO

### Keywords:

Urban landslide  
Monitoring  
Ambient seismic noise  
Inclinometer

## ABSTRACT

Landslides are a major natural hazard, threatening communities and infrastructures worldwide. Mitigation of these hazards relies on understanding their causes and triggering processes, which critically depend on subsurface characteristics and their variations over time. In this study, we present a novel approach combining passive seismic and low-cost inclinometer monitoring methods to improve the understanding of landslide activation mechanisms and their controls. We evaluate the efficiency of this approach on a shallow, slow-moving landslide directly endangering a road bridge, a bridge that is part of an important emergency response route. Results show the value of combining the two approaches for observing and monitoring landslide hazards. Passive seismic monitoring captures the variation in soil properties (rigidity and density) over time by sensing the variations of the seismic wave velocity ( $dV/V$  and its associated correlation coefficient). At the same time, novel low-cost inclinometers are monitoring subsurface deformation (from millimetric to pluricentimetric scale) and temperature. Seismic precursors detected at the bottom sensor a few hours prior to the reactivation are followed by the reactivation of the landslide toe, releasing stresses in the top part that lead to the reactivation of the whole landslide. This reactivation occurs during an episode of heavy rainfall following a 7-month drought. Meanwhile, temperature monitoring enables us to track water infiltration and to highlight its role in the landslide mechanisms. Overall, the combination of the two monitoring methods shows promise for quantifying the sliding mechanisms of landslide reactivations and for designing landslide early warning systems.

## 1. Introduction

Numerous regions of the world are exposed to landslide hazards, which pose problems for land management and population safety (Guzzetti, 2000; Hungr et al., 2014; Panizza et al., 1996; Picarelli et al., 2005). Between 1998 and 2017, landslides affected 4.8 million people and caused over 18,000 deaths (Froude and Petley, 2018). Catastrophic landslide events are often triggered by heavy rainfall, earthquakes, or anthropogenic activities (Lacroix et al., 2020). Monitoring the controlling mechanism of such complex events during failure is difficult, because of their velocity and destructive force. Slow-moving landslides offer an opportunity to better understand these mechanisms, as processes occur at time scales that are easier to observe (Palmer, 2017).

A variety of methods exists to investigate landslide characteristics and dynamics, ranging from point measurements and geophysical investigations at the site scale to remote sensing products applied globally. Combining those methods has been shown to provide valuable insights into landslide processes. Landslide characterization is commonly

performed using geotechnical methods such as cone penetration tests (Solberg et al., 2016), and/or geophysical methods like electrical resistivity tomography (Solberg et al., 2016) or seismic (Bièvre et al., 2016; Uhlemann et al., 2016a). Monitoring of landslide dynamics is done using geotechnical approaches such as inclinometric measurements (Furuya et al., 1999; Jeng et al., 2017; Uhlemann et al., 2016b), remote sensing solutions (Benoit et al., 2015; Carlà et al., 2019; Fiolleau et al., 2021; Lacroix et al., 2018), or geophysical techniques (Fiolleau et al., 2020; Jongmans et al., 2021; Whiteley et al., 2019).

Among those methods, inclinometers have been shown to be reliable and effective in accurately tracking ground deformation, enabling the estimation of the sliding surface depth (with centimetric accuracy) and the displacement rate with centimetric to millimetric accuracy (Gullà et al., 2017; Sass et al., 2008; Uhlemann et al., 2016b). Traditional inclinometers, derived from a prototype built in 1952 by S.D. Wilson (Stark and Choi, 2008), have been commonly used since their commercialization in the 1950s to monitor ground deformation to hundreds of meters in depth. However, the high cost of these systems makes them

<sup>\*</sup> Corresponding author.

E-mail address: [sfiolleau@lbl.gov](mailto:sfiolleau@lbl.gov) (S. Fiolleau).

<https://doi.org/10.1016/j.jappgeo.2023.105090>

Received 23 August 2022; Received in revised form 26 May 2023; Accepted 28 May 2023

Available online 1 June 2023

0926-9851/Published by Elsevier B.V. This is an open access article under the CC BY license (<http://creativecommons.org/licenses/by/4.0/>).

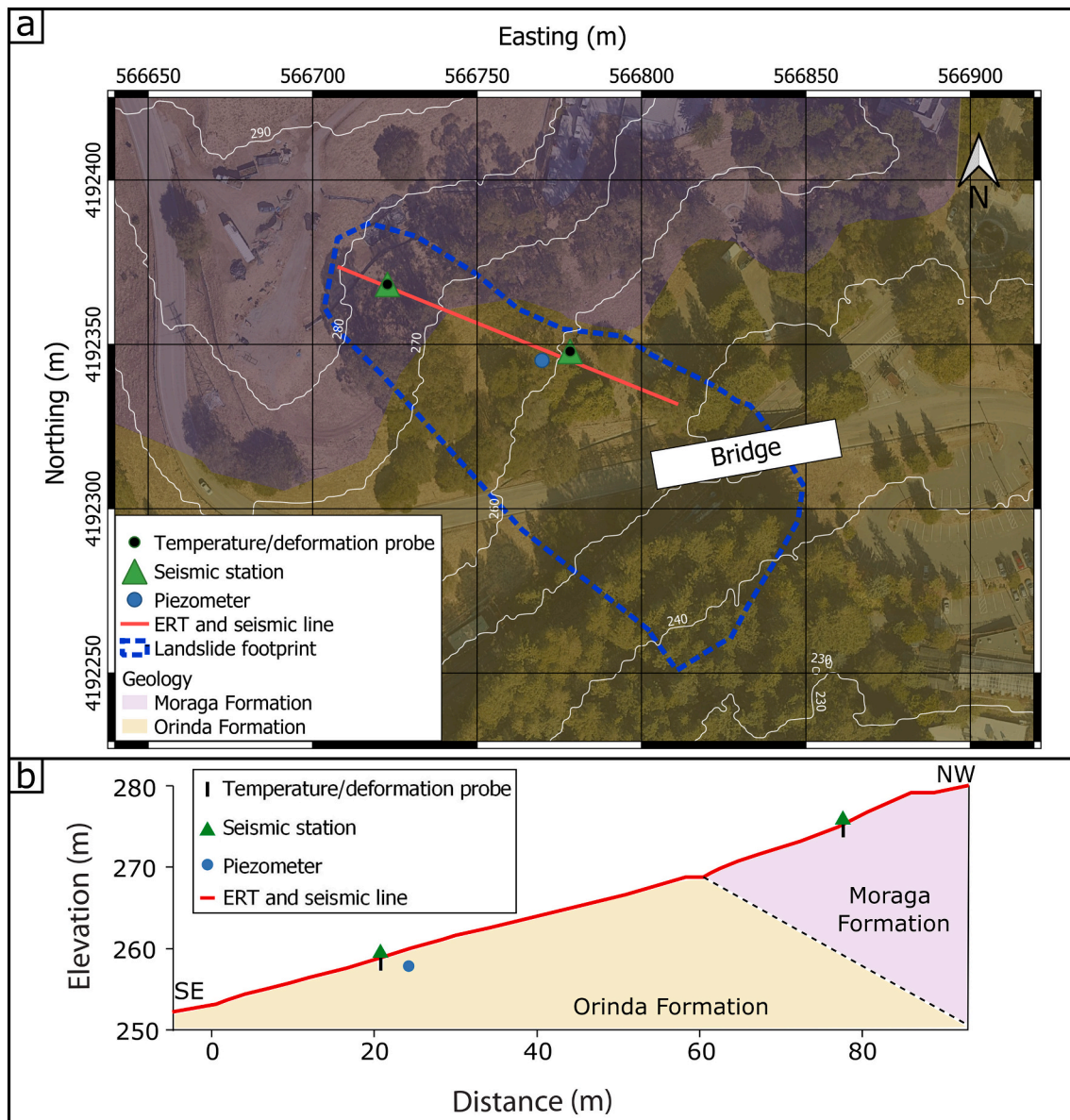


Fig. 1. a) Map showing the landslide footprint. Location of seismic, deformation/temperature probes, piezometer, ERT and seismic line. Geological limits are presented without considering surficial deposits. White lines indicate isoelevations. b) cross section showing location of seismic stations, deformation/temperature probes and piezometer along the ERT and seismic line (following the topography extracted from RTK-GPS measurements).

poorly suited for shallow environments. For this reason, over the past decade, the development of MEMs-based accelerometers for monitoring shallow landslides has largely been used (Abdoun et al., 2013; Ruzza et al., 2020). Recently, Wielandt et al. (2022, 2023) developed low-power sensor arrays combining MEMs and temperature measurements to monitor soil deformation and ground temperature simultaneously at multiple depths. Besides deformation, and among other soil properties, soil temperature is particularly valuable for better constraining the triggering mechanisms of slope instabilities. Shibasaki et al. (2016) investigated the effect of temperature on the residual strength of soil located in slip zones of slow-moving landslides. They showed that for smectite-rich soil, a decrease in temperature will lead to a decrease in shear resistance, which ultimately could trigger a slow-moving landslide. Temperature monitoring at depth can also be used for detecting groundwater flow (Takeuchi, 1980). Furuya et al. (2006) used soil-temperature monitoring combined with slope instability analysis to better understand the relationship between groundwater-vein distribution and slope failures in the Zentoku area, Japan.

Recent studies have shown that temporal changes in seismic wave velocity ( $dV/V$ ) and the associated correlation coefficient (CC) are useful parameters for monitoring soil-property variations and to detect precursors of landslide reactivations (Colombero et al., 2021; Le Breton et al., 2021). Mainsant et al. (2012) detected a drop in Rayleigh wave velocity a few days before a sliding event of the Pont de Bourquin landslide. They interpreted this drop as the result of a decrease in rigidity of the soil. In the above-mentioned studies, seismic wave velocity variations were extracted from the cross-correlation of ambient seismic noise recorded at two different stations. An alternative to investigating seismic velocity variation would be to use the noise single-station cross-components correlation function (NSCF, De Plaen et al., 2016; Machacca-Puma et al., 2019; Wegler and Sens-Schönfelder, 2007), in which only one seismic station is required to monitor  $dV/V$  and CC around a station. Bontemps et al. (2020) used this technique to track and better understand the forcing mechanisms of a slow-moving landslide in Peru.

All the above-mentioned studies show that characterizing landslide

mechanisms and reactivations requires a combination of techniques. To date, some studies have combined methods to understand these mechanisms (Fiolleau et al., 2021; Uhlemann et al., 2016b), but none has simultaneously tracked seismic velocity changes, soil deformation, and temperature variations at multiple depths. This combination of methods could enable major advances in understanding changes in soil properties, water infiltration patterns, and their influence on reactivation mechanisms.

In this study, we combine low-cost deformation and temperature measurements with ambient seismic noise recordings to characterize and monitor a small landslide reactivation caused by an intense rain event. The depth-resolved, distributed measurements of soil deformation enable us to characterize the dynamics of the reactivation of the shallow landslide mass. At the same time, monitoring of shear-wave-velocity variations in the vicinity of the probe deformation measurements makes it possible to characterize the ground disturbances leading up to the destabilization of the soil mass, and to assist in interpreting the displacement measurements.

## 2. Study site

The study site, located in the San Francisco Bay Area on the west side of the northwest-trending Berkeley Hills (Fig. 1), has a significant history of landsliding (Fiolleau et al., 2023). The Hayward and San Andreas faults, which are in close proximity to the study site, are potential sources of seismic activity. The Berkeley Hills bedrock geology is complex, comprising moderately to highly deformed sedimentary, volcanic, and metamorphic rock units. The investigated landslide directly impacts a road bridge that is a crucial part of an evacuation route and has been studied intensively (Uhlemann et al., 2021). The landslide, which can be classified as a very slow moving clay rotational slide (Hungre et al., 2014), is located within a paleolandslide deposit (up to 18 m thick) composed of weathered Moraga formation (mainly weathered basalt and andesite flows), overlying the Orinda formation (non-marine, conglomerate sandstone, and green and red mudstone). Previous geotechnical studies of the site showed that soil and bedrock have, respectively, an effective cohesion of about 8 kPa and 120 kPa, a unit weight of about 14 kN/m<sup>3</sup> and 19 kN/m<sup>3</sup>, and a friction angle of about 24° and 40° (Kropp Alan and Associates, 2006). Since 2012, the ground displacement is monitored using a deeply anchored (2 m deep) GPS station. This station indicates movement rates of up to about 10 mm/year, with movements predominantly occurring during precipitation events (Cohen-Waeber, 2018). Unfortunately, the GPS station stopped working during the studied event, which prevented us from using it.

## 3. Materials and methods

### 3.1. Characterization

The characterization of the subsurface was performed using two geophysical methods: seismic refraction tomography (SRT) and electrical resistivity tomography (ERT) (Fig. 1). The geophysical data were interpreted based on a nearby borehole log (A3GEO, Inc., 2020).

The seismic data were acquired using 48 geophones with 2 m spacing. Vertical geophones with a 4.5 Hz eigen frequency were used for the P-wave survey. The source was a 4.5 kg sledge hammer hitting a horizontal metallic plate. Horizontal geophones with a 4.5 Hz eigen frequency were used for the S-wave survey, and a steel prism with 45° inclined faces placed perpendicular to the profile was used to generate S-waves with opposing polarizations (Uhlemann et al., 2016a). In both cases, the same shot locations were used, and shots were stacked to improve the signal-to-noise ratio; the number of stacks varied based on the environmental noise conditions.

The ERT transect included 64 electrodes 1.5 m apart. The data were acquired using dipole-dipole measurements, with a dipole length  $a$  of 1.5, 3.0, 4.5, 6.0, 7.5, and 9 m, and a dipole spacing  $n$  of 1 to 8a. To

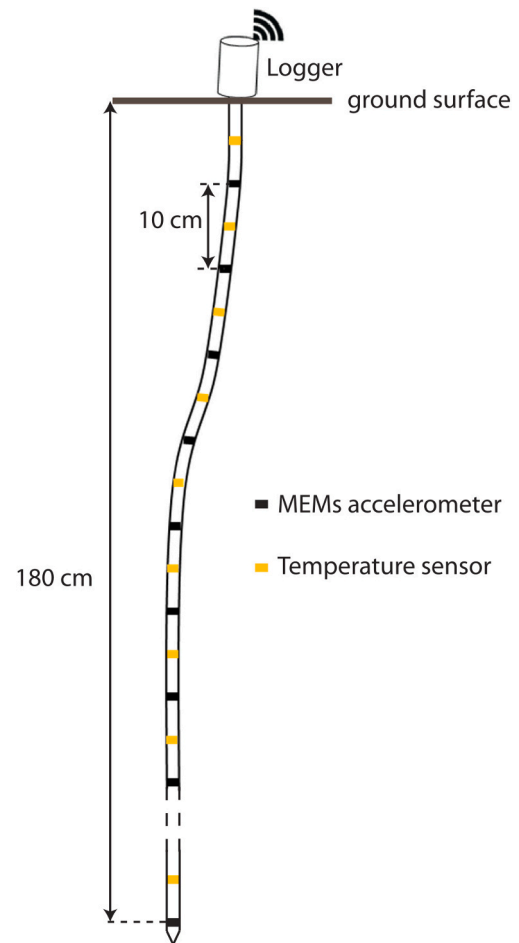


Fig. 2. Design of the probe with temperature sensors and accelerometers.

assess the measurement error, a full set of reciprocal data was acquired, and showed very good data quality. Based on the reciprocal errors, a linear error model was developed (Tso et al., 2017) with a relative error of 0.2%, and an absolute error of 0.0001 Ohm.

To fully exploit the sensitivities of the P- and S-wave seismic refraction and electrical resistivity tomographic data, we used a structurally coupled cooperative joint inversion approach (Skibbe et al., 2021; Wagner and Uhlemann, 2021), which was implemented in PyGIMLi (Rücker et al., 2017). In this approach, the structural similarity is achieved by smoothness constraints in the regularization operator that are locally decreased based on the roughness of the model, and updated between iterations. This approach enables the exchange of structural information between p- and s-wave seismic refraction and electrical resistivity tomography data, and allows us to focus on common boundaries. The P and S-wave seismic refraction tomography data were used to infer the elastic moduli and the Poisson's ratio, which are known to provide crucial information for understanding landslide processes (Uhlemann et al., 2016a). The Poisson's ratio, a good indicator of the saturation of the subsurface, is derived from the inverted  $V_p$  and  $V_s$  profiles using

$$\nu = \frac{V_p^2 - 2V_s^2}{2(V_p^2 - V_s^2)} \quad (1)$$

### 3.2. Monitoring

The landslide was monitored with two shallow inclinometer arrays (Wielandt et al., 2022), two seismic stations, and a piezometer (Fig. 1) from July 26 to October 31, 2021. During this period, the data were

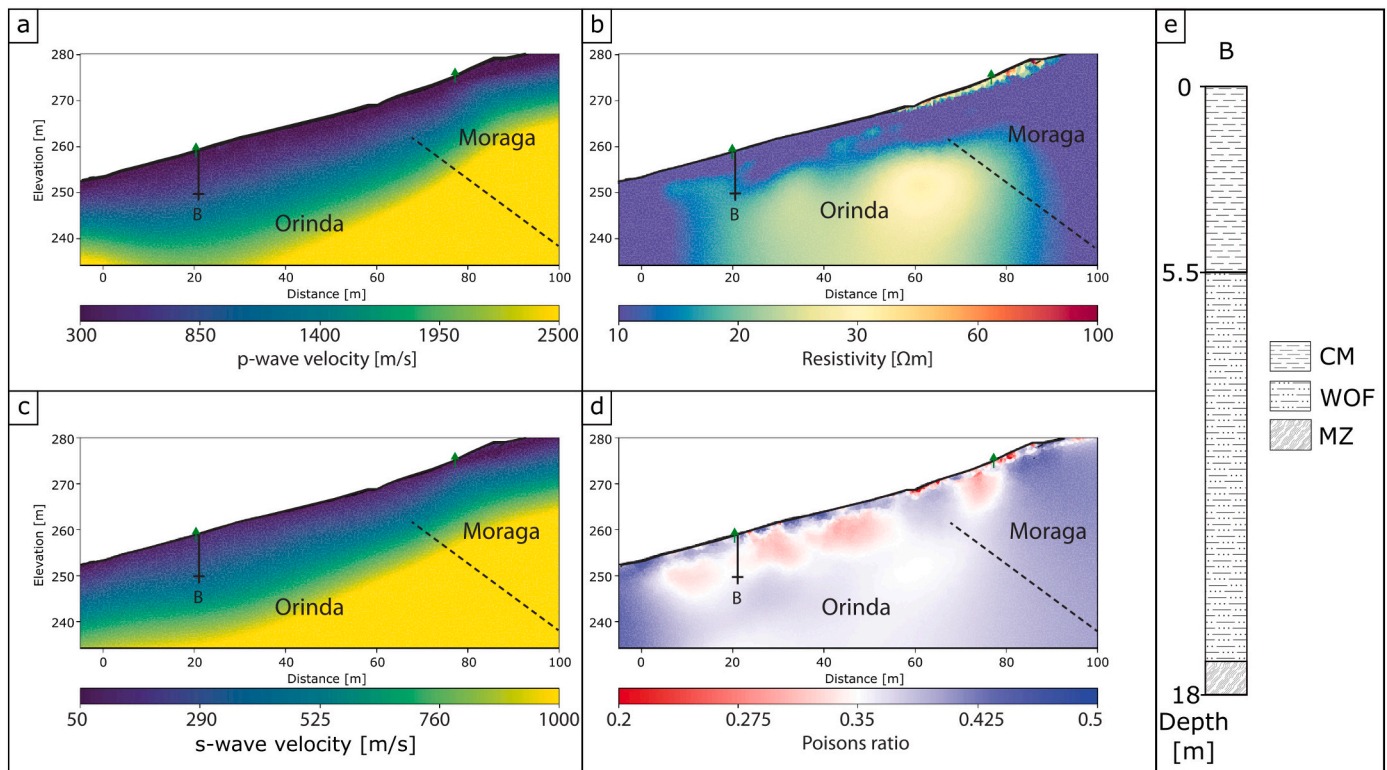


**Fig. 3.** Geophysical profiles overlaid with borehole (B) location, the position of the seismic stations (green triangle) and inclinometer arrays (green line). a)  $V_p$ , b) ERT, c)  $V_s$ , d) Poisson's ratio profiles and e) borehole log with stiff clay material (CM), weak Orinda Formation (WOF) and Mineralization zone (MZ). The interpreted contact between Moraga and Orinda formation is highlighted by the black dot line. (For interpretation of the references to colour in this figure legend, the reader is referred to the web version of this article.)

acquired autonomously without any major interruption except from the beginning of August to October 19 for the seismic data. This study focused primarily on the major rainstorm event starting on October 24.

Each inclinometer array was 1.8 m long (Fig. 2), composed of 18 three-component MEMS accelerometers (first sensor at 10 cm depth) and 18 temperature sensors, which were placed alternately at 5 cm intervals (Fig. 2). A low-cost, AA battery-powered data logger was used to record the MEMS and temperature measurements continuously at a sampling rate of 15 min (Wielandt and Dafflon, 2021). The deformation in the horizontal plane was extracted from the inclinometric measurements with submillimetric accuracy following Wielandt et al. (2022).

The air temperature, rainfall, and wind time-series were retrieved from the Lawrence Berkeley National Laboratory's weather station (Horel et al., 2002), located 700 m away from the studied landslide (not visible on the map). The station records each parameter every 15 min. The water table dynamics were monitored by a piezometer installed to 1.8 m depth, located between the two seismic stations and the two inclinometers (Fig. 1), with a sampling rate of 30 min.

The two seismic stations were collocated with the two inclinometers (Fig. 1). The three-component geophones with an eigen frequency of 4.5 Hz were oriented (NW) along the slope gradient and recorded seismic ambient noise at a sampling rate of 200 Hz. The NSCF of the ambient seismic noise were calculated to track potential changes in Rayleigh wave velocity. First, the Fourier spectra of 1 h recordings were normalized for each frequency value (spectral whitening) to ensure a similar statistical contribution of all frequencies in the considered frequency range (3–50 Hz). Secondly, these 1 h recordings of the different components at each station were cross-correlated (East-Vertical, North-Vertical and East-North). Then, the method consisted of comparing each cross-correlogram to a reference, by a new correlation, to detect a variation in seismic wave velocity (extension or retraction of the signal, change in  $dV/V$ ) or a variation in signal shape (change of CC). A moving

reference cross-correlogram was computed by averaging all hourly cross-correlograms over a 48 h period preceding the hourly cross-correlogram considered. All the correlograms were bandpass filtered for center frequencies between 3 and 50 Hz over a bandwidth of 2 Hz and in steps of 0.5 Hz. Then, hourly velocity changes with respect to the considered reference correlogram were calculated for the different frequency bands, using the stretching technique (Lobkis and Weaver, 2003; Sens-Schönfelder and Wegler, 2006) for the time window [0.05–4 s] in the coda. This time window was sufficient to account for all scattered waves in the investigated volume. This technique enabled an analysis of the velocity variation ( $dV/V$ ) and the associated correlation coefficient (CC).

## 4. Results

### 4.1. Subsurface characteristics

$V_p$  and  $V_s$  profiles show low seismic velocities in the first 1.5 m, of 300 m/s and 80 m/s, respectively (Fig. 3a and c). A high Poisson's ratio is present in the lower part of the profile (0 to 60 m, Fig. 3d) in the upper 1.5 m depth, highlighting the presence of a fully saturated layer. At the top of the slope, the relatively high resistivity values (above 30  $\Omega\text{m}$ , Fig. 3b) and a low Poisson's ratio (around 0.2, Fig. 3d) highlight the presence of a very weak and porous shallow layer of about 1.5 m thickness. These results are consistent with the geology at the site, in particular the presence of a rocky permeable deposit from the Moraga formation at the top of the slope, and a stiff clayey material with a low permeability at the bottom. The seismic velocity increases with depth and reaches 2500 m/s and 1000 m/s at 20 m depth for  $V_p$  and  $V_s$ , respectively. The seismic velocities are consistent with the geotechnical investigation. Indeed, the 18 m deep borehole shows the presence of stiff clay (CM, Fig. 3e) in the first 5.5 m. Below, highly weathered siltstone

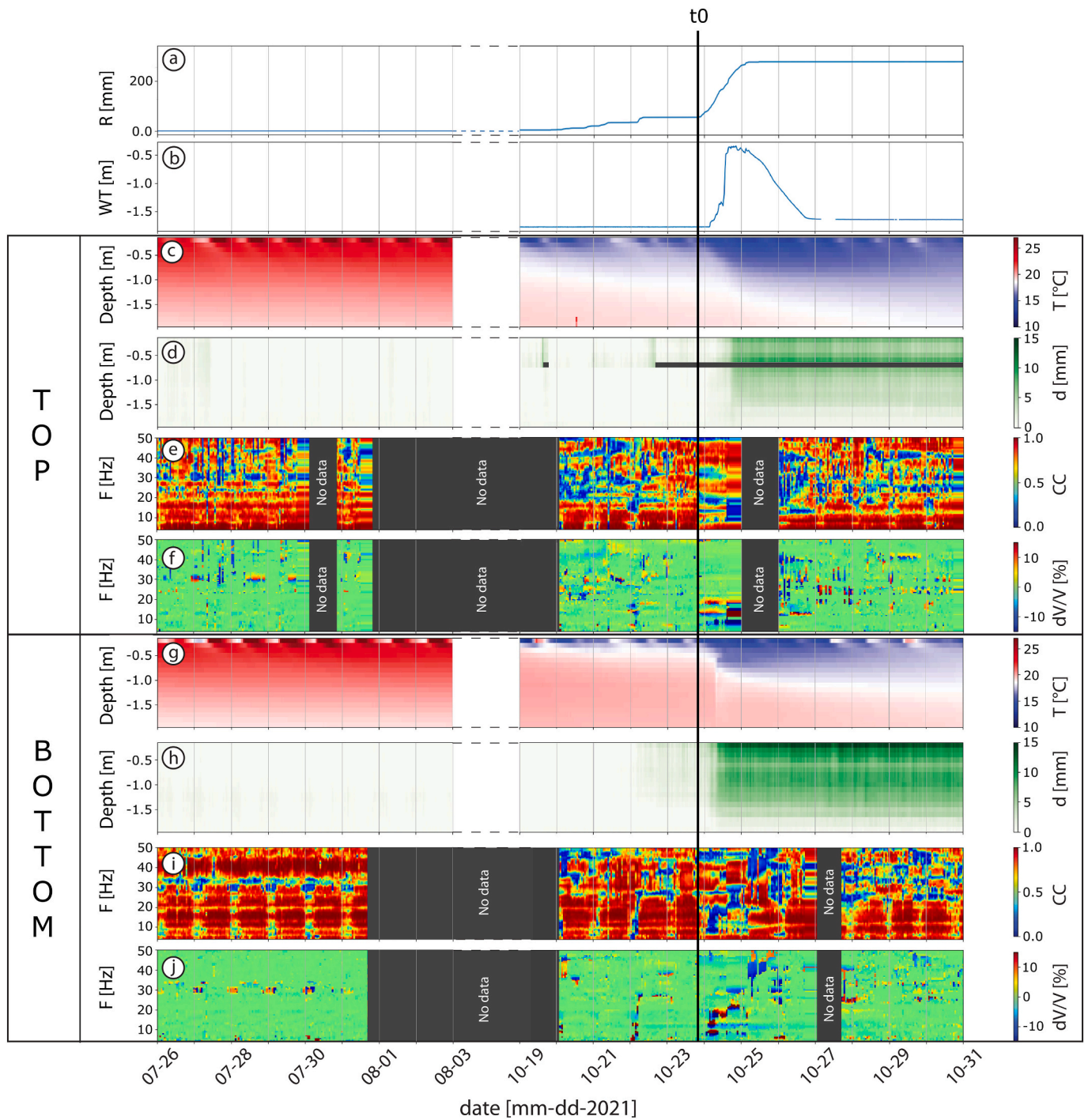


**Fig. 4.** Monitoring data from July 26 to October 31: a) rainfall amount (R, [mm]), b) Water table level (WT, [m]), and subsurface data at the (c-f) top and (g-j) bottom of the landslide. c,g) temperature [°C], d,h) displacement [mm], e,i) Correlation coefficient (from 4 to 50 Hz), f,j) seismic waves velocity variations (from 4 to 50 Hz) (dV/V, [%]). No data is indicated in grey. T<sub>0</sub> indicates the beginning of the rainstorm event.

(Orinda formation, WOF, Fig. 3e) is observed until reaching a mineralization zone at 17–18 m depth corresponding to the end of the borehole (MZ, Fig. 3e). At around 60 m along the profile, a low Poisson’s ratio, from the surface to about 2 m depth, corresponds to lower water content probably due to the presence of coarser material, and hence higher permeability. This agrees with shallow soil cores, which showed stiff clay starting at depths of about 1.6 to 2.0 m. Then, the Poisson’s ratio becomes higher, likely corresponding to a higher water content. This probably correspond to a change in soil type from coarse to clayey soil, which can store water and then would explain the low Poisson’s ratio in

deeper areas.

#### 4.2. Landslide dynamics

The landslide dynamics during summer (July 26 to August 1) and fall (October 19 to October 31) periods are evaluated based on variations in water table level (Fig. 4b), soil temperature, Fig. 4c and g), soil displacement (Fig. 4d and h), seismic wave velocity (Fig. 4f and j), and the associated correlation coefficient (Fig. 4e and i). The summer period is characterized by the absence of rain (Fig. 4a) and landslide events, and

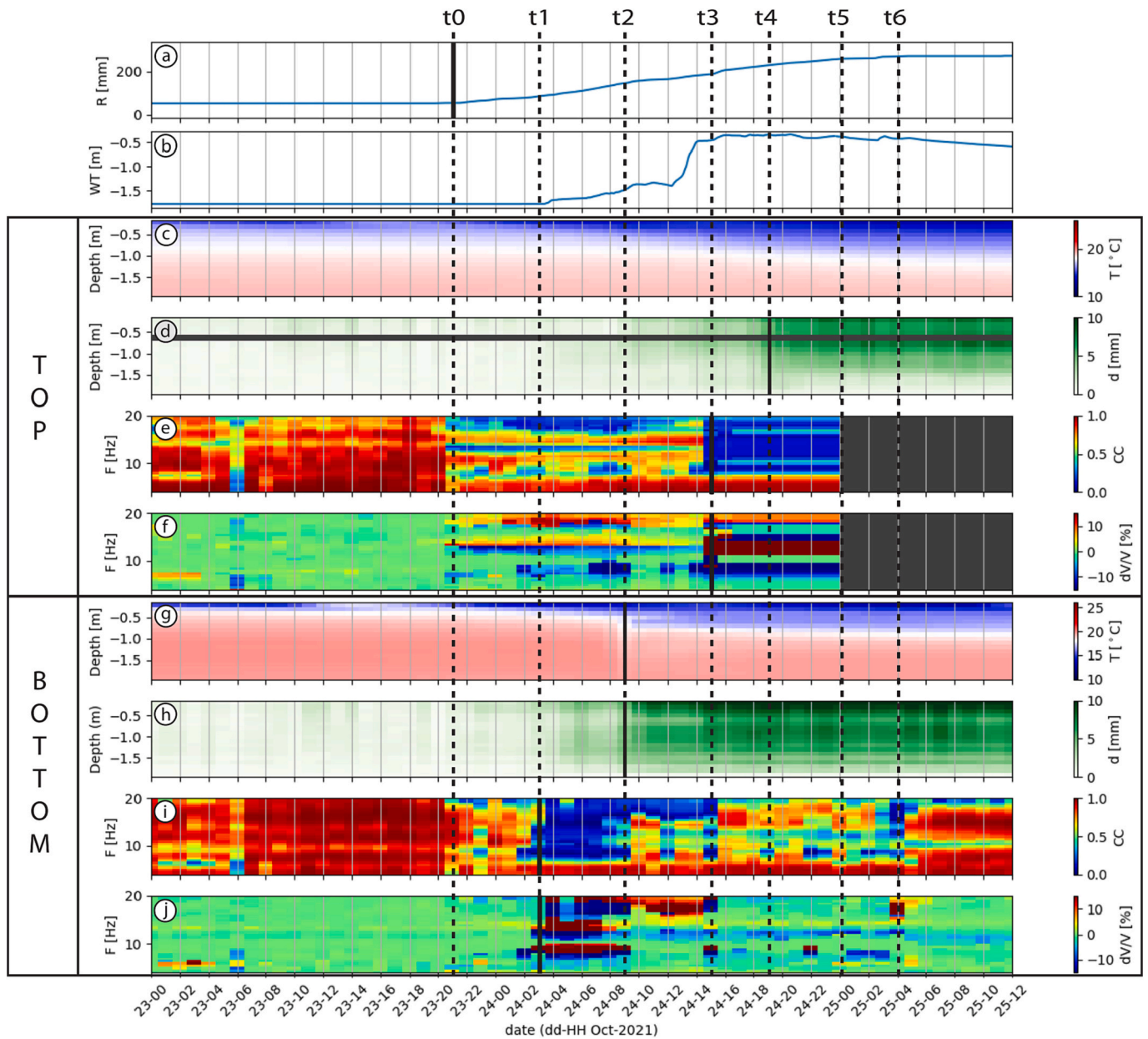


**Fig. 5.** Monitoring data from October 23 to October 25: a) rainfall amount (R, [mm]), b) Water table level (WT, [m]), and subsurface data at the (c-f) top and (g-j) bottom of the landslide. c,g) temperature [°C], d,h) displacement [mm], e,i) Correlation coefficient (from 4 to 50 Hz), f,j) seismic wave velocity variations (from 4 to 20 Hz) (dV/V, [%]). Dashed line highlights time  $t_n$  ( $n = 1-6$ ), continuous line highlights which parameter reacts. No data is indicated in grey.

a water table depth remaining deeper than 1.8 m. The inclinometer arrays indicate very little to no change in soil temperature and displacements during this period. In addition, no seismic velocity variations are observed and the associated correlation coefficient (CC) is high.

The fall period encompasses a large rainstorm event, starting on October 23, bringing about 220 mm of rain in 30 h. This major event triggered a small reactivation, resulting in a displacement of a few millimeters. Seismic, deformation, and temperature measurements show a clear response during this event. Temperature measurements indicate different infiltration patterns at the top and bottom of the slope. The gradual decrease in temperature with depth at the top highlights the infiltration process into the subsurface, while the rapid decrease in temperature at the bottom of the slope indicates rapid infiltration along the probe, preventing the infiltration pattern into the subsurface from being observed.

The seismic monitoring shows the evolution of dV/V and the

associated CC during the rainstorm event, reflecting changes in soil properties (rigidity and/or density). Before the rainstorm event, CC remains low, with some fluctuations at high frequencies (sensitive to the first centimeters of soil) during small rainfall events. At the time of the rainstorm event, a drop in CC at low frequencies between 7 and 20 Hz and deformation of about 1 cm at 1.5 m depth are observed at the top and bottom of the slope. A few days after the end of the rainstorm event, displacement halts, the CC increases to its initial level for all frequencies and at the top and bottom of the slope. Although the seismic wave velocity variations (dV/V) also drop during the rainstorm event, this drop in dV/V cannot be interpreted because of the low value of CC.

**Figs. 5 and 6** highlight the landslide dynamic during the rainstorm period in more detail. The rainfall event started on October 23 (t0, Fig. 5) at 8 p.m. At the same time, a drop in CC occurred between 15 and 20 Hz at the top and around 20 Hz at the bottom. A few hours later, the CC at the bottom of the slope drops between 7 and 20 Hz (t1, October 24,

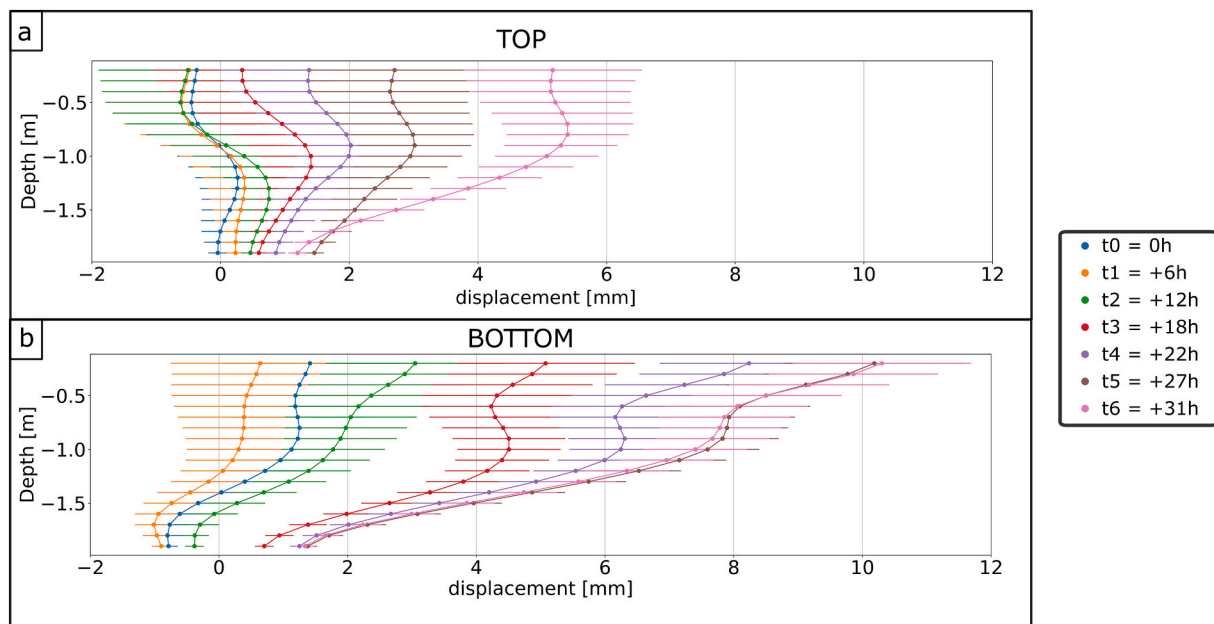
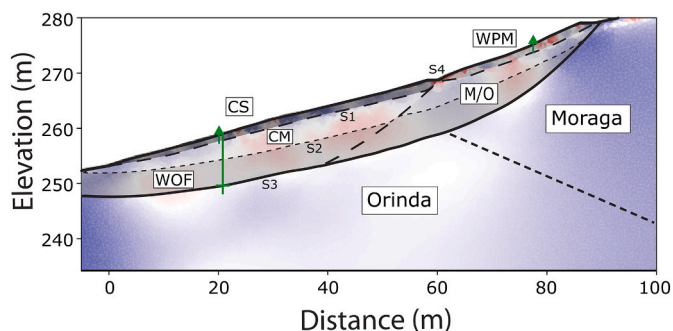


Fig. 6. Displacements with error bars recorded by the inclinometer at the top (a) and at the bottom (b) of the landslide at time  $t_n$  ( $n = 1-6$ ) defined in Fig. 5.



- CS : Stiff clayey saturated layer
- CM : Stiff clayey material
- WOF : Weathered Orinda formation
- WPM: Weak and porous deposit from Moraga formation
- M/O : Landslide deposit mix Moraga/Orinda formations

Fig. 7. Interpretative cross-section of the landslide. The borehole and instrumentations positions are highlighted in green. (For interpretation of the references to colour in this figure legend, the reader is referred to the web version of this article.)

2 a.m., Fig. 5i). The measured displacements remain below the noise level (of about  $\pm 1$  mm, Wielandt et al., 2022). The cumulative amount of rain reached 25 mm. On October 24 at 8 a.m. ( $t_2$ , Fig. 5), the soil temperature in the top 1.5 m of soil quickly decreases, likely resulting from water infiltration along the probe and related advective and conductive heat transfer. At the same time, a displacement of 3 mm is recorded by the bottom inclinometer array (Fig. 5h and 6b) along the shallow sliding surface at about 1.6 m depth (October 24, 9 a.m., Fig. 5). The water-level sensor shows a considerable rise in water level on October 24 between 12 p.m. to 2 p.m. The cumulative amount of rain reached 94 mm at 2 p.m. on October 24. At this time ( $t_3$ , Fig. 5) CC at the top of the slope drops between 10 and 20 Hz (October 24, 3 p.m., Fig. 5e), and the water table reaches its highest level ( $-0.4$  m), with a cumulative amount of rain reaching 135 mm. The displacement in the bottom part reaches 5 mm (Figs. 5h and 6b). At 6 p.m. on October 24 ( $t_4$ , Fig. 5), a displacement of about 2 mm (Figs. 5d and 6a) is recorded at the

top of the slope at about 1.6 m depth, indicating the presence of a sliding surface. At 11 p.m. on October 24 ( $t_5$ , Fig. 5) both inclinometer arrays show displacements of up to 10 mm and 3 mm at the bottom and the top of the slope, respectively (+27 h, Fig. 6). ( $t_6$ ) The bottom inclinometer array shows no sign of displacement on the shallow sliding surface (+36 h, Fig. 6b), while the top inclinometer array indicates a total displacement of 5 mm.

## 5. Discussion

### 5.1. Geological layers and sliding surfaces

The combination of borehole logging and geophysical profiles lead to a better understanding of the landslide structure (Fig. 7). Based on the various datasets, we interpreted four sliding surfaces (S1, S2, S3, S4) with S4 starting at the surface and splitting the landslide in two parts. The presence of S4 at the ground surface is suggested by a topographic depression at about 60 m along the profile (Fig. 3). The angle of the sliding surface has been interpreted as the continuity of the surface slope angle. The upper soil layer consists of a superficial, stiff, clayey saturated layer (CS) at the bottom of the landslide (0 to 60 m), and a rocky, porous deposit (from the Moraga formation, WPM) at the top of the landslide, both sliding on S1, located at about 1.5 m depth (Figs. 6 and 7). At the bottom of the landslide, stiff clay (CM) is present between S1 and S2 and is overlying highly weathered siltstone (WOF, Orinda formation), with their interface at 5.5 m depth (S2). The borehole and the Poisson's ratio (0.2–0.3, Fig. 3) show that the Orinda formation is highly fractured and weathered (WOF) between 5.5 and 18 m depth, corresponding to the depth of the paleolandslide (S3), as interpreted in previous studies (A3GEO, Inc., 2020). In the top part of the landslide, the geology below WPM is likely composed of a mix of weathered material from Orinda and Moraga formations (M/O). Three sliding surfaces were interpreted; however, the poor resistance of the Orinda formation (WOF and M/O) down to 18 m depth probably leads to numerous interconnected sliding surfaces.

### 5.2. Rainstorm induced reactivation

The rainstorm event occurring in October 2021 triggered a small reactivation of the landslide. Fig. 8 illustrates the main episodes of this



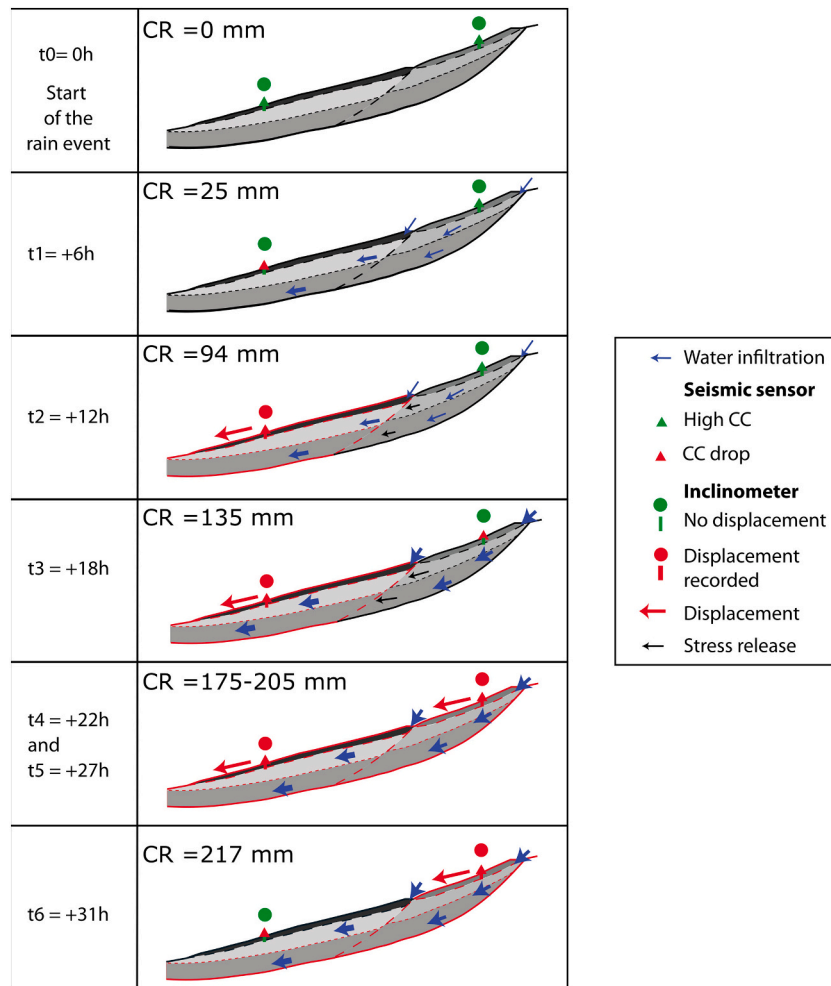


**Fig. 8.** interpretative cross-sections of the event. CR: cumulative rainfall. Circles and line show if a displacement is detected (red) or not (green) by the inclinometer. The size of the infiltration arrows highlights the relative amount of water infiltrated.

event, highlighting specific mechanisms. The rainstorm event started on October 23 at 8 p.m. (Fig. 8, t0). The CC at the bottom of the landslide dropped 6 h later (Fig. 8, t1) between 7 Hz and 20 Hz, which corresponds to a depth range of approximately 15 m to 1 m considering the s-wave velocities (Fig. 3, from 50 to 250 m/s). This drop shows that the material started to saturate (increasing pore pressure) from superficial to deeper layers through water infiltration. Twelve hours after the rainstorm started (t2), the inclinometer at the bottom showed displacements of 3 mm, while the top inclinometer was still static (in noise level, Fig. 6a). The bottom part of the slope likely moved along S4 and S3, exhibiting a displacement at the surface of a few cm, with the top layer (CS) moving a few mm (up to 10 mm) on S1, as shown by the inclinometer. This displacement released stresses in the top part of the slope, reworking the material located there (WPM and M/O). At the same time, the water table rose to its highest level (0.4 m depth), leading to increasing pore-water pressure. The combination of the two phenomena led (6 h later, t3), to a drop in CC between 10 and 20 Hz at the top. Then, 22 h after the rainstorm started (t4), the higher part triggered, with the shallow layer exhibiting 2 mm displacement. The entire landslide exhibited a displacement during 9 h, with the shallow layer moving the fastest, up to 10 mm at the bottom (Fig. 6b, t5) and 5 mm at the top of the landslide (Fig. 6a, t6). At the bottom of the landslide, the shallow layer stopped moving relative to the deeper layers, 31 h after the rainstorm started (Fig. 6b, t6). However, since the CC was still low, between 7 and 20 Hz, the deeper sliding surfaces were likely still active.

A few days after the rainstorm event (October 29), the increase in CC

at both sensor locations highlighted the end of the event. An increase in CC means that the reference and the correlogram at the considered time  $t$  are getting closer. Considering that we have a moving reference, it means that the disturbances have stopped with no more reworking of the material. The CC detects the end of the event on October 27 (10-20 Hz at the top, Fig. 4e), corresponding to the stabilization of the water table level at 1.6 m depth.

### 5.3. Potential and limitations of the proposed approach

This paper details the combination of inclinometric, temperature, and seismic measurements to characterize the reactivation of shallow slow-moving landslides. The inclinometer array showed a high capacity for tracking millimeter displacements, even with high temperature variations (Wielandt et al., 2022), and its combination with temperature measurements enabled us to highlight the influence of water infiltration on those displacements. Several hours prior to the reactivation period, ambient seismic noise, and more precisely CC, reacted to changes in water content. Given that landslide mechanisms are driven by water circulation, seismic ambient noise parameters would seem to be key components to monitor from an early warning perspective. This has been highlighted here and in other studies (Fiolleau et al., 2020; Mainsant et al., 2012), which show that seismic-noise-derived parameters (like  $dV/V$  or CC) may change hours prior to landslide reactivation. In those cases, ambient noise has been applied to deep seated landslides. The methodology we proposed, combining shallow inclinometer and

ambient seismic noise is well suited in the case of shallow landslides, but also for deeper landslide with additional shallow sliding surfaces (as in this case).

While this study has shown the value of combining displacement, temperature, and ambient noise monitoring, many steps are still needed to move from test case to a widely deployable strategy. One of the current limitations of the inclinometer network is its inability to capture total displacement at the surface if it is not anchored in the bedrock. However, we are still able to detect differential displacement between shallow and deeper layers. Uhlemann et al. (2016b) also showed the usefulness of unanchored inclinometers to track deformation and slip depth, although the results should be interpreted with caution. In this regard, additional combinations of GPS monitoring systems and/or remote sensing products (InSAR, image correlations) are promising. Importantly, increasing the density and coverage of these measurements is possibly achievable, because of the relatively low cost of passive seismic methods and inclinometer arrays. Data management can be similarly optimized through the development of automated data processing, edge computing, and connected wireless sensor networks (Wielandt et al., 2022). The relatively simple algorithms required to process and combine the above-mentioned datasets could be applied in real time on edge devices, providing real-time measures of CC, displacement, and temperature that could be readily integrated into IoT landslide early warning systems.

## 6. Conclusion

In this study, we presented the characterization and monitoring of a slow-moving landslide directly endangering a bridge that is a critical component of an emergency evacuation route within a highly populated area. We demonstrated the value of combining inclinometers, temperature, hydrological, and seismic data to improve the understanding of landslide mechanisms within an early warning context. Vertically resolved temperature measurements showed water infiltration patterns in both types of materials, confirming its influence on reactivation mechanisms in the shallow subsurface. The ambient seismic-noise monitoring allowed us to track changes in the medium due to water infiltration a few hours prior to the actual reactivation. Low-cost inclinometric measurements, providing displacement information with millimeter accuracy, enabled a precise assessment of the displacement in the top layer. Overall, the multimethod approach applied here enables a comprehensive understanding of the reactivation mechanism, highlighting that the lower part reactivated first owing to fast water infiltration, releasing stresses at the top of the landslide, allowing the entire landslide to finally reactivate. This study focused on a very small reactivation after a short, but intense, rainstorm event. It clearly shows the potential of this multimethod approach, which will be used in the future to continuously monitor landslide dynamics with higher spatial resolution and across a wider range of reactivation intensity. With respect to its early warning potential, we believe this approach will provide reliable detection of precursors to potentially risky landslide reactivations.

## Funding

This research has been supported by the Laboratory Directed Research and Development Program of Lawrence Berkeley National Laboratory under U.S. Department of Energy Contract No. DE-AC02-05CH11231.

## CRediT authorship contribution statement

**Fiolleau Sylvain:** Conceptualization, Data curation, Formal analysis, Methodology, Writing – original draft, Writing – review & editing. **Dafflon Baptiste:** Supervision, Writing – review & editing. **Wielandt Stijn:** Resources. **Uhlemann Sebastian:** Funding acquisition, Project administration, Supervision, Writing – original draft, Writing – review &

editing.

## Declaration of Competing Interest

The authors declare that they have no known competing financial interests or personal relationships that could have appeared to influence the work reported in this paper.

## Data availability

Data will be made available on request.

## References

- A3GEO, Inc, 2020. *Geotechnical Data and Interpretations Report Fiscal Year 2020*. Ground Motions Study Lawrence Berkeley National Laboratory Berkeley, California.
- Abdoun, T., Bennett, V., Desrosiers, T., Simm, J., Barendse, M., 2013. Asset management and safety assessment of levees and earthen dams through comprehensive real-time field monitoring. *Geotech. Geol. Eng.* 31, 833–843. <https://doi.org/10.1007/s10706-012-9569-3>.
- Benoit, L., Briole, P., Martin, O., Thom, C., Malet, J.-P., Ulrich, P., 2015. Monitoring landslide displacements with the geocube wireless network of low-cost GPS. *Eng. Geol.* 195, 111–121. <https://doi.org/10.1016/j.enggeo.2015.05.020>.
- Bièvre, G., Jongmans, D., Goutaland, D., Pathier, E., Zumbo, V., 2016. Geophysical characterization of the lithological control on the kinematic pattern in a large clayey landslide (Avignonet, French Alps). *Landslides* 13, 423–436. <https://doi.org/10.1007/s10346-015-0579-0>.
- Bontemps, N., Lacroix, P., Larose, E., Jara, J., Taïpe, E., 2020. Rain and small earthquakes maintain a slow-moving landslide in a persistent critical state. *Nat. Commun.* 11, 1–10. <https://doi.org/10.1038/s41467-020-14445-3>.
- Carlà, T., Tofani, V., Lombardi, L., Raspini, F., Bianchini, S., Bertolo, D., Thuegatz, P., Casagli, N., 2019. Combination of GNSS, satellite InSAR, and GBInSAR remote sensing monitoring to improve the understanding of a large landslide in high alpine environment. *Geomorphology* 335, 62–75. <https://doi.org/10.1016/j.geomorph.2019.03.014>.
- Cohen-Waerber, J.F., 2018. *Spatiotemporal Patterns of Seasonality in Landslide Deformation from InSAR and GPS* (Ph.D.). University of California, Berkeley, United States – California.
- Colombero, C., Jongmans, D., Fiolleau, S., Valentin, J., Baillet, L., Bièvre, G., 2021. Seismic noise parameters as indicators of reversible modifications in slope stability: a review. *Surv. Geophys.* 42, 339–375. <https://doi.org/10.1007/s10712-021-09632-w>.
- De Plaen, R.S.M., Lecocq, T., Caudron, C., Ferrazzini, V., Francis, O., 2016. Single-station monitoring of volcanoes using seismic ambient noise. *Geophys. Res. Lett.* 43, 8511–8518. <https://doi.org/10.1002/2016GL070078>.
- Fiolleau, S., Jongmans, D., Bièvre, G., Chambon, G., Baillet, L., Vial, B., 2020. Seismic characterization of a clay-block rupture in Harmalière landslide, French Western Alps. *Geophys. J. Int.* 221, 1777–1788. <https://doi.org/10.1093/gji/ggaa050>.
- Fiolleau, S., Jongmans, D., Bièvre, G., Chambon, G., Lacroix, P., Helmstetter, A., Wathelet, M., Demierre, M., 2021. Multi-method investigation of mass transfer mechanisms in a retrogressive clayey landslide (Harmalière, French Alps). *Landslides*. <https://doi.org/10.1007/s10346-021-01639-z>.
- Fiolleau, S., Uhlemann, S., Falco, N., Dafflon, B., 2023. Assessing probability of failure of urban landslides through rapid characterization of soil properties and vegetation distribution. *Geomorphology* 423, 108560. <https://doi.org/10.1016/j.geomorph.2022.108560>.
- Froude, M.J., Petley, D., 2018. Global fatal landslide occurrence from 2004 to 2016. *Nat. Hazards Earth Syst. Sci.* 18, 2161–2181. <https://doi.org/10.5194/nhess-18-2161-2018>.
- Furuya, G., Sassa, K., Hiura, H., Fukuoka, H., 1999. Mechanism of creep movement caused by landslide activity and underground erosion in crystalline schist, Shikoku Island, Southwestern Japan. *Eng. Geol.* 53, 311–325. [https://doi.org/10.1016/S0013-7952\(98\)00084-2](https://doi.org/10.1016/S0013-7952(98)00084-2).
- Furuya, G., Suemine, A., Sassa, K., Komatsubara, T., Watanabe, N., Marui, H., 2006. Relationship between groundwater flow estimated by soil temperature and slope failures caused by heavy rainfall, Shikoku Island, southwestern Japan. *Eng. Geol.* 85, 332–346. <https://doi.org/10.1016/j.enggeo.2006.03.002>.
- Gullà, G., Peduto, D., Borrelli, L., Antronico, L., Fornaro, G., 2017. Geometric and kinematic characterization of landslides affecting urban areas: the lungro case study (Calabria, Southern Italy). *Landslides* 14, 171–188. <https://doi.org/10.1007/s10346-015-0676-0>.
- Guzzetti, F., 2000. Landslide fatalities and the evaluation of landslide risk in Italy. *Eng. Geol.* 58, 89–107. [https://doi.org/10.1016/S0013-7952\(00\)00047-8](https://doi.org/10.1016/S0013-7952(00)00047-8).
- Horel, J., Split, M., Dunn, L., Pechmann, J., White, B., Ciliberti, C., Lazarus, S., Slemmer, J., Zaff, D., Burks, J., 2002. MESOWEST: cooperative mesonets in the Western United States. *Bull. Am. Meteorol. Soc.* 83, 211–226. [https://doi.org/10.1175/1520-0477\(2002\)083<0211:MCMTW>2.3.CO;2](https://doi.org/10.1175/1520-0477(2002)083<0211:MCMTW>2.3.CO;2).
- Hung, O., Leroueil, S., Picarelli, L., 2014. The Varnes classification of landslide types, an update. *Landslides* 11, 167–194. <https://doi.org/10.1007/s10346-013-0436-y>.
- Jeng, C.-J., Yo, Y.-Y., Zhong, K.-L., 2017. Interpretation of slope displacement obtained from inclinometers and simulation of calibration tests. *Nat. Hazards* 87, 623–657. <https://doi.org/10.1007/s11069-017-2786-6>.

- Jongmans, D., Fiolleau, S., Bièvre, G., 2021. Geophysical monitoring of landslides: State-of-the-art and recent advances. In: Casagli, N., Tofani, V., Sassa, K., Bobrowsky, P.T., Takara, K. (Eds.), *Understanding and Reducing Landslide Disaster Risk, Monitoring and Early Warning*, vol. 3. ICL Contribution to Landslide Disaster Risk Reduction. Springer International Publishing, Cham, pp. 75–84. [https://doi.org/10.1007/978-3-030-60311-3\\_7](https://doi.org/10.1007/978-3-030-60311-3_7).
- Kropp Alan, Associates, 2006. *Initial landslide characterization study East Canyon-Buildings 85 and 85A*.
- Lacroix, P., Bièvre, G., Pathier, E., Kniess, U., Jongmans, D., 2018. Use of Sentinel-2 images for the detection of precursory motions before landslide failures. *Remote Sens. Environ.* 215, 507–516. <https://doi.org/10.1016/j.rse.2018.03.042>.
- Lacroix, P., Hantzwerger, A., Bièvre, G., 2020. Life and death of slow-moving landslides. *Nat. Rev. Earth Environ.* 1 (8), 404–419. <https://doi.org/10.1038/s43017-020-0072-8>.
- Le Breton, M., Bontemps, N., Guillemot, A., Baillet, L., Larose, É., 2021. Landslide monitoring using seismic ambient noise correlation: challenges and applications. *Earth-Sci. Rev.* 216, 103518 <https://doi.org/10.1016/j.earscirev.2021.103518>.
- Lobkis, O.I., Weaver, R.L., 2003. Coda-wave interferometry in finite solids: recovery of P-to-S conversion rates in an elastodynamic billiard. *Phys. Rev. Lett.* 90, 254302 <https://doi.org/10.1103/PhysRevLett.90.254302>.
- Machacca-Puma, R., Lesage, P., Larose, E., Lacroix, P., Ancasi-Figueroa, R.M., 2019. Detection of pre-eruptive seismic velocity variations at an andesitic volcano using ambient noise correlation on 3-component stations: Ubinas volcano, Peru, 2014. *J. Volcanol. Geotherm. Res.* 381, 83–100. <https://doi.org/10.1016/j.jvolgeores.2019.05.014>.
- Mainsant, G., Larose, E., Brönnimann, C., Jongmans, D., Michoud, C., Jaboyedoff, M., 2012. Ambient seismic noise monitoring of a clay landslide: toward failure prediction. *J. Geophys. Res.* 117, F01030. <https://doi.org/10.1029/2011JF002159>.
- Palmer, J., 2017. Creeping earth could hold secret to deadly landslides. *Nature* 548, 384–386. <https://doi.org/10.1038/548384a>.
- Panizza, M., Pasuto, A., Silvano, S., Soldati, M., 1996. Temporal occurrence and activity of landslides in the area of Cortina d'Ampezzo (Dolomites, Italy). *Int. J. Rock Mech. Min. Sci. Geomech. Abstr.* 33, 311–326. [https://doi.org/10.1016/S0148-9062\(97\)87272-5](https://doi.org/10.1016/S0148-9062(97)87272-5).
- Picarelli, L., Urciuoli, G., Ramondini, M., Comegna, L., 2005. Main features of mudslides in tectonised highly fissured clay shales. *Landslides* 2, 15–30. <https://doi.org/10.1007/s10346-004-0040-2>.
- Rücker, C., Günther, T., Wagner, F.M., 2017. pyGIMLi: an open-source library for modelling and inversion in geophysics. *Comput. Geosci.* 109, 106–123. <https://doi.org/10.1016/j.cageo.2017.07.011>.
- Ruzza, G., Guerriero, L., Revellino, P., Guadagno, F.M., 2020. A multi-module fixed inclinometer for continuous monitoring of landslides: design, development, and laboratory testing. *Sensors* 20, 3318. <https://doi.org/10.3390/s20113318>.
- Sass, O., Bell, R., Glade, T., 2008. Comparison of GPR, 2D-resistivity and traditional techniques for the subsurface exploration of the Öschingen Landslide, Swabian Alb (Germany). *Geomorphol. Challenges Geomorphol. Methods Tech.* 93, 89–103. <https://doi.org/10.1016/j.geomorph.2006.12.019>.
- Sens-Schönfelder, C., Wegler, U., 2006. Passive image interferometry and seasonal variations of seismic velocities at Merapi Volcano, Indonesia. *Geophys. Res. Lett.* 33 <https://doi.org/10.1029/2006GL027797>.
- Shibasaki, T., Matsuura, S., Okamoto, T., 2016. Experimental evidence for shallow, slow-moving landslides activated by a decrease in ground temperature. *Geophys. Res. Lett.* 43, 6975–6984. <https://doi.org/10.1002/2016GL069604>.
- Skibbe, N., Günther, T., Müller-Petke, M., 2021. Improved hydrogeophysical imaging by structural coupling of 2D magnetic resonance and electrical resistivity tomography. *GEOPHYSICS* 86. <https://doi.org/10.1190/geo2020-0593.1>. WB77–WB88.
- Solberg, I.-L., Long, M., Baranwal, V.C., Gylland, A.S., Rønning, J.S., 2016. Geophysical and geotechnical studies of geology and sediment properties at a quick-clay landslide site at Esp, Trondheim, Norway. *Eng. Geol.* 208, 214–230. <https://doi.org/10.1016/j.enggeo.2016.04.031>.
- Stark, T.D., Choi, H., 2008. Slope inclinometers for landslides. *Landslides* 5, 339. <https://doi.org/10.1007/s10346-008-0126-3>.
- Takeuchi, A., 1980. Method of investigating groundwater-vein streams by measuring one-meter-depth temperature in landslide areas part 1. *J. Jpn. Assoc. Groundw. Hydrol.* 22, 73–101. <https://doi.org/10.5917/jagh1959.22.73>.
- Tso, C.-H.M., Kuras, O., Wilkinson, P.B., Uhlemann, S., Chambers, J.E., Meldrum, P.I., Graham, J., Sherlock, E.F., Binley, A., 2017. Improved characterisation and modelling of measurement errors in electrical resistivity tomography (ERT) surveys. *J. Appl. Geophys.* 146, 103–119. <https://doi.org/10.1016/j.jappgeo.2017.09.009>.
- Uhlemann, S., Hagedorn, S., Dashwood, B., Maurer, H., Gunn, D., Dijkstra, T., Chambers, J., 2016a. Landslide characterization using P- and S-wave seismic refraction tomography — the importance of Elastic Moduli. *J. Appl. Geophys.* 134, 64–76. <https://doi.org/10.1016/j.jappgeo.2016.08.014>.
- Uhlemann, S., Smith, A., Chambers, J., Dixon, N., Dijkstra, T., Haslam, E., Meldrum, P., Merritt, A., Gunn, D., Mackay, J., 2016b. Assessment of ground-based monitoring techniques applied to landslide investigations. *Geomorphology* 253, 438–451. <https://doi.org/10.1016/j.geomorph.2015.10.027>.
- Uhlemann, S., Chambers, J., Meldrum, P., McClure, P., Dafflon, B., 2021. Geophysical monitoring of landslides—a step closer towards predictive understanding? In: Casagli, N., Tofani, V., Sassa, K., Bobrowsky, P.T., Takara, K. (Eds.), *Understanding and Reducing Landslide Disaster Risk, Monitoring and Early Warning*, vol. 3. ICL Contribution to Landslide Disaster Risk Reduction. Springer International Publishing, Cham, pp. 85–91. [https://doi.org/10.1007/978-3-030-60311-3\\_8](https://doi.org/10.1007/978-3-030-60311-3_8).
- Wagner, F.M., Uhlemann, S., 2021. Chapter one - An overview of multimethod imaging approaches in environmental geophysics. In: Schmelzbach, C. (Ed.), *Advances in Geophysics, Inversion of Geophysical Data*. Elsevier, pp. 1–72. <https://doi.org/10.1016/bs.agph.2021.06.001>.
- Wegler, U., Sens-Schönfelder, C., 2007. Fault zone monitoring with passive image interferometry. *Geophys. J. Int.* 168, 1029–1033. <https://doi.org/10.1111/j.1365-246X.2006.03284.x>.
- Whiteley, J.S., Chambers, J.E., Uhlemann, S., Wilkinson, P.B., Kendall, J.M., 2019. Geophysical monitoring of moisture-induced landslides: a review. *Rev. Geophys.* 57, 106–145. <https://doi.org/10.1029/2018RG000603>.
- Wielandt, S., Dafflon, B., 2021. Minimizing power consumption in networks of environmental sensor arrays using TDD LoRa and delta encoding. In: 2021 55th Asilomar Conference on Signals, Systems, and Computers. Presented at the 2021 55th Asilomar Conference on Signals, Systems, and Computers, pp. 318–323. <https://doi.org/10.1109/IEEECONF53345.2021.9723227>.
- Wielandt, S., Uhlemann, S., Fiolleau, S., Dafflon, B., 2022. Low-power, flexible sensor arrays with solderless board-to-board connectors for monitoring soil deformation and temperature. *Sensors* 22, 2814. <https://doi.org/10.3390/s22072814>.
- Wielandt, S., Uhlemann, S., Fiolleau, S., Dafflon, B., 2023. TDD LoRa and delta encoding in low-power networks of environmental sensor arrays for temperature and deformation monitoring. *J. Sign. Process Syst.* <https://doi.org/10.1007/s11265-023-01834-2>.